SCIENTIFIC
Publishing Limited

Bio-Robotics
http://ojs.ukscip.com/index.php/br

Article

Synthetic Analysis on Radar Cross-Section and Remote Sensing for an Ornithopter

Zeyang Zhou * and **Jun Huang**

School of Aeronautic Science and Engineering, Beihang University, Beijing 100191, China
* Correspondence: zeyangzhou@buaa.edu.cn

Received: 13 April 2025; **Revised:** 28 May 2025; **Accepted:** 5 June 2025; **Published:** 11 June 2025

Abstract: To learn remote sensing features and radar cross-section (RCS) of a biorobotics ornithopter, a conjoint analysis approach built on remote sensing imaging and dynamic electromagnetic scattering is presented. The fuselage model of this flapping-wing aircraft adopts a low-scattering configuration design, with a pair of wings located on both sides of the front fuselage. High-fidelity unstructured mesh technology is utilized to model the surfaces of wings and fuselage. Linear transformation is employed in analyzing remote sensing grayscale, and dynamic electromagnetic scattering methods are applied to obtain the RCS of objects. The results show that this method can acquire the remote sensing grayscale characteristics of the ground and the ornithopter; however, the presence of some ground objects makes it difficult for flapping-wing machines to be identified. Compared to the forward case, there are more azimuths in the lateral direction, which are beneficial in reducing the average and peak indicators of the dynamic RCS of the ornithopter. Considering the case of tail incidence, the peak and mean RCS of the ornithopter show a tendency to first decrease and then grow within a given range. Low-grayscale water bodies and boundary areas with significant grayscale differences are advantageous for quickly identifying the ornithopter.

Keywords: Remote Sensing Modeling; Dynamic Electromagnetic Scattering; Flapping Wing; Joint Analysis; Radar Stealth

1. Introduction

Remote sensing platforms can observe ground objects, surface vessels, and low altitude aircraft from high altitude. Flapping-wing aircraft mainly rely on wing flutter to generate lift and thrust, and can fly between obstacles such as forests and hills. It has the characteristics of high bionics and good concealment, and is an attractive direction for future aircraft. Learning the radar characteristics of flapping-wing can promote the stealth design and development of birdlike aircraft [1–3].

Different from fixed wing planes and aircraft with rotors, an ornithopter has the advantages of good concealment, flexibility, and strong mobility. Flapping wings can change their movement direction and trajectory by changing their flapping trajectory and attitude [4]. A flexible structural layout and well-designed wing shape can improve the thrust and lift characteristics of an ornithopter [5]. The influence of rocker arm stroke on the lift and drag characteristics of biomimetic dragonflies is discussed [6]. The ornithopter relies on the small motor fixed on the fuselage to provide power to force its wings to flutter up and down [7]. Pigeons often use variable frequency and variable amplitude modes to control wing flutter and torsion in order to achieve the purpose of efficient flight [8]. The biological data of a large flying fox is studied, and the aerodynamic results of a bat-like drone are analyzed [9].

https://doi.org/10.54963/br.v1i1.1363

The seagull is selected as the bionic object to design a two-stage ornithopter simulating the flight motion of birds [10]. The impact of blade flapping and pitching movements on aerodynamics and stealth cannot be ignored [11]. With the deepening of flapping wing research and the development of electromagnetic analysis technology [12,13], future flapping-wing aircraft can fly more efficiently and stealthily.

Electromagnetic scattering calculation requires that the complex target surface be discretized into several plane surface elements and edge approximation grids; thus, the accuracy of target radar cross-section (RCS) calculation depends on the topological mesh data of surface fitting [14,15]. The physical optics (PO) is used to calculate the scattering contribution of the panel, and the equivalent electromagnetic current algorithm is implemented to solve the edge diffraction [15,16]. The quasi-static principle is exploited to simulate the periodic motion of the rotor [17]. A multi-axis dynamic scattering approach is established to determine the RCS of a helicopter with a compound layout [18]. Computational fluid dynamics is used to study the wing kinematics and corrugation structures of an ornithopter [19]. RCS of a set of scattering sources is investigated by the array synthesis formula and numerical simulation [20,21]. The ejection parameters of carrier-based aircraft have been modeled and analyzed [22]. The RCS of convex triangular and cylindrical origami surfaces is calculated using the method of moments (MOM). The flow field of a flapping low-aspect-ratio ellipsoidal-wings has been established and analyzed [23]. Based on interpolating the kernel functions, each kernel function can be expressed in the form of a separation of spatial and temporal variables [24]. The aerodynamic features of a bionic feather drone in gusty environments have been analyzed [25]. An aircraft configuration with two fuselages and ultra-high aspect ratio wings is described [26]. The stealth characteristics of flapping wing aircraft with two different wing shapes are compared [27]. A deformable unmanned aerial vehicle capable of changing sweep angle and wing span is presented [28]. Biomimetic objects such as large birds, moths, and bats can provide a variety of flight mode references, including hovering, forward flying, inverted flying, and gliding [29–31]. Transient modeling [32,33] is crucial for determining the dynamic electromagnetic scattering of objects with complex motion. Elastic wings [34–36] are of great significance in the design and production of flapping wing drones and flying insects. Overall, the exploration of electromagnetic scattering characteristics of an ornithopter in specific flight modes will face challenges.

As mentioned, there is a lack of research on using remote sensing technology to observe flapping wing aircraft. Conventional flapping-wing aircraft mimic the shape of birds for camouflage, while this bulging fuselage can easily become a stable static scattering source. Different flapping and waving movements cause complex changes in the electromagnetic scattering features of the ornithopter. Therefore, it is difficult to determine the RCS change caused by flapping wings. A wing that remains stationary during taxiing will increase this static scattering contribution, while a flapping wing will form a dynamic scattering outcome and change ornithopter RCS in real time. When the body attitude angle, the pitching and flapping angle of the wing are given, it is necessary to solve the electromagnetic scattering features of the ornithopter in order to analyze RCS results at typical azimuths. This paper endeavours to set up a conjoint analysis method to learn RCS characteristics and remote sensing features of an ornithopter designed with low scattering characteristics. This study has engineering usefulness for the stealth design and remote sensing observation of the flapping-wing machine.

In this paper, the research technique is presented in Section 2. Models are given in Section 3. The result discussion has been completed as shown in Section 4. Finally, the full content is summarized.

2. Conjoint Analysis Method

The draft of remote sensing and RCS analysis for the ornithopter is illustrated in **Figure 1**, where the radar station adopted to observe the electromagnetic scattering features is depicted as a ground-based radar vehicle or a low-altitude radar platform. Remote sensing equipment is installed on high-altitude airships to detect ground and low altitude flapping wing targets. Low-altitude radar and high-altitude airships can jointly observe target flapping wing aircraft.

2.1. Remote Sensing Imaging

When the narrow pulse wave transmitted by the sensor of the airship is returned by the ornithopter surface at a certain moment, the distance can be determined based on the time difference:

$$R = \frac{1}{2}(t_2 - t_1) \cdot c \tag{1}$$

where *c* is the speed of propagation of electromagnetic waves. t_1 is the time of transmission. *R* refers to the distance between the ornithopter and the sensor. t_2 stands for the time of reception.

The sketch of the projection difference of the sensor image is presented in **Figure 2**, where *H* is the height of the airship sensor. Δh stands for the height of position *P*.

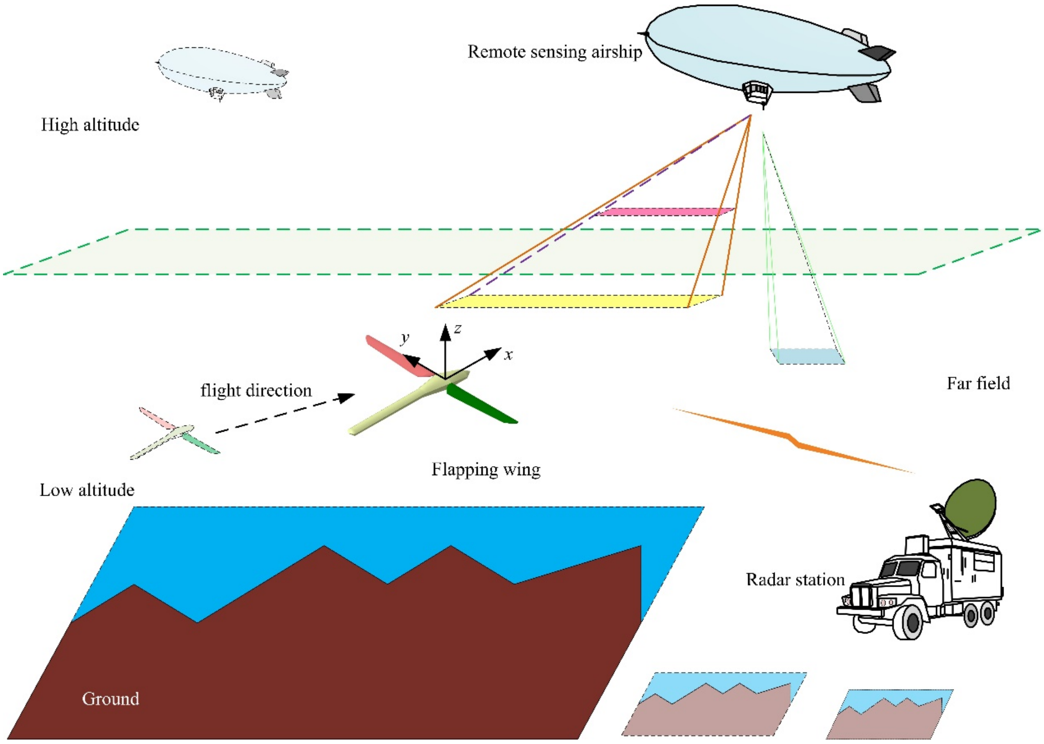

Figure 1. Conjoint analysis schematic of remote sensing and RCS for the flapping wing aircraft.

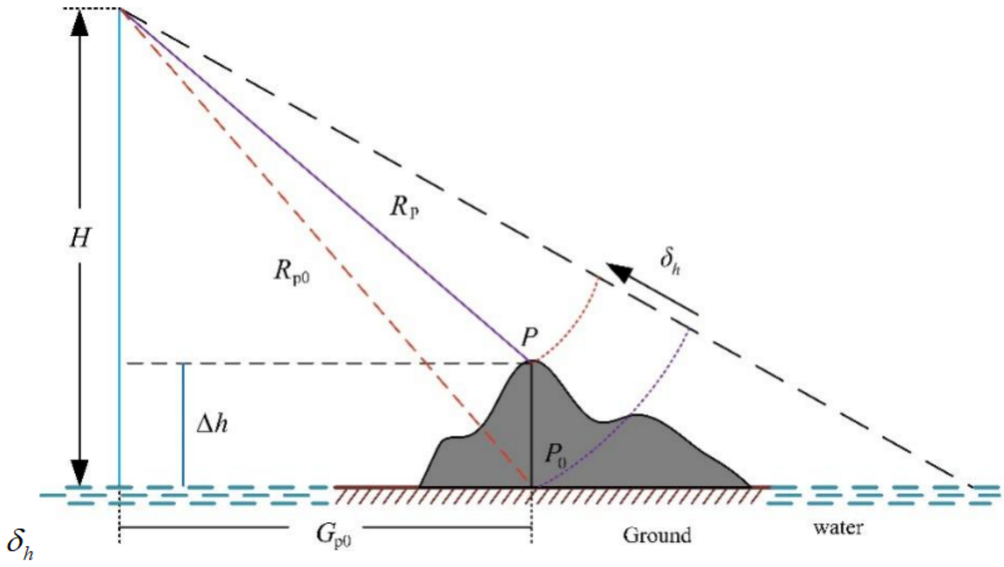

Figure 2. Schematic of projection difference in remote sensing imaging.

Then the projection difference can be calculated as:

$$\delta_h = R_{P0} - R_P \tag{2}$$

where is the projection difference, and R_P means the distance from the sensor to point P.

Noting the following relationship,

$$G_P{}^2 = R_P{}^2 - (H - \Delta h)^2 \tag{3}$$

$$G_P{}^2 = R_{P0}{}^2 - H^2 \tag{4}$$

Then the following expression could be obtained,

$$R_{P0}{}^2 - H^2 = -H^2 + 2H\Delta h - \Delta h^2 + R_P{}^2 \tag{5}$$

$$R_{P0}{}^2 - R_P{}^2 = 2H\Delta h - \Delta h^2 \tag{6}$$

$$(R_{P0} + R_P)(R_{P0} - R_P) = (R_{P0} + 2R_P - R_P)\delta_h = 2H\Delta h - \Delta h^2 \tag{7}$$

$$(\delta_h + 2R_P)\delta_h - 2H\Delta h + \Delta h^2 = 0 \tag{8}$$

The projection difference can be obtained:

$$\delta_h = -R_P \pm \sqrt{R_P{}^2 - \Delta h^2 + 2H\Delta h} \tag{9}$$

Considering that $\delta_h << R_{\mathrm{P}}$, therefore,

$$\delta_h = -R_P + \sqrt{R_P{}^2 - \Delta h^2 + 2H\Delta h} \tag{10}$$

For making remote sensing presentation easier to recognize, picture transformation and enhancement techniques are exploited. For the movement and transformation of the image,

$$X_{\mathrm{ct}} = X_{\mathrm{c0}} + \Delta X_{\mathrm{c}} \tag{11}$$

$$Y_{\mathrm{ct}} = Y_{\mathrm{c0}} + \Delta Y_{\mathrm{c}} \tag{12}$$

where (X_{c0},Y_{c0}) represents the original coordinates of the reference point. (X_{ct}, Y_{ct}) refers to the coordinates of the transformed reference point. For the changes in image grayscale,

$$G_{\mathrm{t}} = G_{tn} + \frac{G_{\mathrm{t}m} - G_{\mathrm{t}n}}{G_{0m} - G_{0n}}(G_0 - G_{0n}) \tag{13}$$

where G_0 means the original image grayscale. G_{t} is the picture grayscale after linear transformation, the additional subscripts 'm' and 'n' representing the maximum and minimum values. This ornithopter can repeatedly conduct independent flights so that high-altitude remote sensing airships can observe the target area multiple times.

2.2. Dynamic RCS Assessment

The sketch of electromagnetic scattering of the ornithopter is shown in **Figure 3**, where f_{rh} denotes the radar wave frequency as well as horizontal polarization. A_{f} is the flapping angle, and the extra numeric subscript indicates the wing number. α is azimuth, β is elevation angle. A_{p} is the pitching angle, and the extra numerical subscript is adopted to differentiate between different wings. The calculation approach utilized to analyze the RCS of this ornithopter mainly includes two parts: electromagnetic scattering evaluation and the dynamic transformation module.

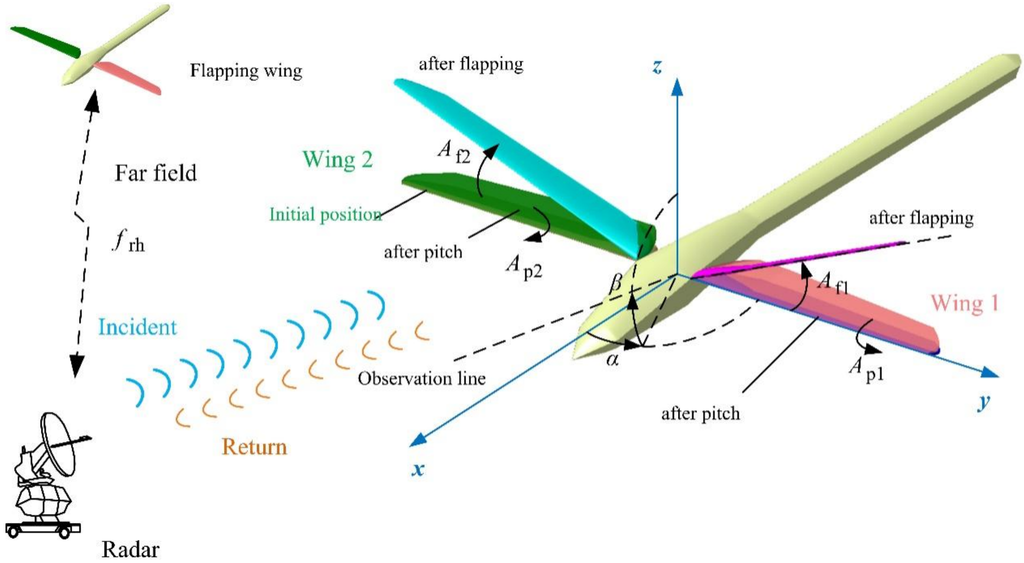

Figure 3. Draft of electromagnetic scattering of the biorobotics ornithopter.

This analysis module is established to acquire the ornithopter RCS at a given instantaneous state. The wings and fuselage of this ornithopter are designed with low scattering features. When evaluating the contribution of panel scattering, the electric and magnetic fields could be determined according to the PO method:

$$\boldsymbol{E}(\boldsymbol{r}) = \frac{1}{j\omega\varepsilon \cdot 4\pi} \iint_{S_I(t)} [2\boldsymbol{J}_s(\boldsymbol{r}')\frac{1+jkR}{R^3}e^{-jkR} + \frac{3-k^2R^2+j3kR}{R^5}e^{-jkR}\boldsymbol{R}\times(\boldsymbol{R}\times\boldsymbol{J}_s(\boldsymbol{r}'))]\mathrm{d}S \tag{14}$$

$$\boldsymbol{H}(\boldsymbol{r}) = \frac{1}{4\pi} \iint_{S_I(t)} \frac{-1-jkR}{R^3}e^{-jkR}(\boldsymbol{R}\times\boldsymbol{J}_s(\boldsymbol{r}'))\mathrm{d}S \tag{15}$$

where ω is the angular frequency of the electromagnetic wave. $\boldsymbol{J}_{\rm s}$ is surface induced current. R denotes the distance between the field point and the source point. $\boldsymbol{r}'$ is the coordinate vector of the source point. k is the wave number in free space. $\boldsymbol{r}$ is the coordinate vector of the field point. dS stands for integral facet. ε refers to dielectric permittivity. $\boldsymbol{R}$ means the distance vector between the field point and the source point.

In view of the assumption of the PO method, the surface current can be expressed as:

$$\boldsymbol{J}_s = \begin{cases} 2\boldsymbol{n}\times\boldsymbol{H} & ,S_I \\ \boldsymbol{0} & ,S_D \end{cases} \tag{16}$$

where $\boldsymbol{n}$ is the unit normal vector of the outer direction of $\boldsymbol{r}'$ at the object surface.

When the fuselage is fastened in the current observation system:

$$\boldsymbol{M}_{\rm flap}(t) = [\boldsymbol{M}_{\rm w1}(t), \boldsymbol{M}_{\rm w2}(t), \boldsymbol{M}_{\rm f}(t=0)] \tag{17}$$

Where t is time, $\boldsymbol{M}_{\rm flap}$ refers to the grid coordinate matrix of the flapping machine. $\boldsymbol{M}_{\rm f}$ means the grid coordinate matrix of the fuselage. $\boldsymbol{M}_{\rm w1}$ denotes the grid coordinate matrix of wing 1. $\boldsymbol{M}_{\rm w2}$ is the grid coordinate matrix of wing 2.

Considering that the ornithopter has many edge features, the physical theory of diffraction (PTD) is applied to compute the edge contribution. Therefore, the dynamic RCS of the whole aircraft can be obtained in the following form:

$$\sigma(t) = \left|\sum_{j=1}^{N_E(t)} (\sqrt{\sigma_E(t)})_j + \sum_{i=1}^{N_F(t)} (\sqrt{\sigma_F(t)})_i\right|^2, \quad t \in [0, T_{obs}] \tag{18}$$

where σ means RCS, subscript F stands for facet contribution, and mark E denotes edge contribution. $N_{\rm F}$ is the number of facets. $N_{\rm E}$ is the number of edges. $T_{\rm obs}$ denotes the observation time limit:

$$T_{\rm obs} \geq T_{\rm flap} \tag{19}$$

where T_{flap} is the flapping period. For a more detailed description of transient RCS assessment, please refer to the literature papers [18,20].

The flight mode of this ornithopter includes gliding mode and flapping mode, and this analysis module aims to generate the pitching angle and flapping angle, and dynamically update the whole flapping wing model. Considering the flapping mode, the pitching angle changes as given below:

$$A_{\mathrm{f1}}(t) = A_{\mathrm{k1}} \sin(\omega_{\mathrm{k1}} t + B_{\mathrm{k1}}) + C_{\mathrm{k1}} \quad , t \in [0, \ \frac{T_{\mathrm{flap}}}{2}) \tag{20}$$

where A_{k}, B_{k}, ω_{k}, and C_{k} are the coefficients, additional numerical marks are used to differentiate various time periods, noting that the incipient flapping direction is upward.

During the second half stage of wing flutter:

$$A_{\mathrm{f1}}(t) = A_{\mathrm{k2}} \sin(\omega_{\mathrm{k2}} t + B_{\mathrm{k2}}) - C_{\mathrm{k2}} \quad , t \in [T_{\mathrm{flap}}/2, \ \ T_{\mathrm{flap}}) \tag{21}$$

For the pitching angle:

$$A_{\mathrm{p1}}(t) = \begin{cases} \theta_{\mathrm{up}} & , \ t \in [0, \ \ T_{\mathrm{flap}}/4) \cup [3T_{\mathrm{flap}}/4, \ \ T_{\mathrm{flap}}) \\ \theta_{\mathrm{down}} & , \ t \in [T_{\mathrm{flap}}/4, \ \ 3T_{\mathrm{flap}}/4) \end{cases} \tag{22}$$

where θ_{up} is the pitching angle when the wing flutters upward, and θ_{down} denotes the pitching angle when it flutters down.

When the flapping wing aircraft is in gliding mode, the flapping angle of wing 1 is kept at a fixed value:

$$A_{\mathrm{f1}} = \varphi_0, \quad \varphi_0 \in [0, \ \ \varphi_{\mathrm{m}}] \tag{23}$$

where φ_0 is a preset angle, φ_{m} denotes the limit value of the flapping angle. At this time, the pitching angle remains unchanged:

$$A_{\mathrm{p1}} = \theta_0, \quad \theta_0 \in [0, \ \ \theta_{\mathrm{m}}] \tag{24}$$

where θ_0 is a given value, θ_{m} is the boundary value of the pitch angle.

When wing 1 is pitching as shown in **Figure 4**, the matrix of facet (F_{w1}) changes as follows:

$$\forall P_i = [x(P_i), y(P_i), z(P_i)]^T \in F_{w1} | i = 1, 2, ..., N_{\mathrm{f},w1} \tag{25}$$

$$\forall F_{w1} \in \boldsymbol{M}_{w1}(t = 0) \tag{26}$$

$$\boldsymbol{M}(F_{w1}(A_{\mathrm{p}}, t)) = \begin{bmatrix} \cos A_{\mathrm{p1}}(t) & 0 & -\sin A_{\mathrm{p1}}(t) \\ 0 & 1 & 0 \\ \sin A_{\mathrm{p1}}(t) & 0 & \cos A_{\mathrm{p1}}(t) \end{bmatrix} \cdot \boldsymbol{M}(F_{w1}(t = 0)) \tag{27}$$

where P_i denotes a facet vertex, $N_{\mathrm{f,w1}}$ is the number of wing 1 facets, and $\boldsymbol{M}$ is the coordinate matrix.

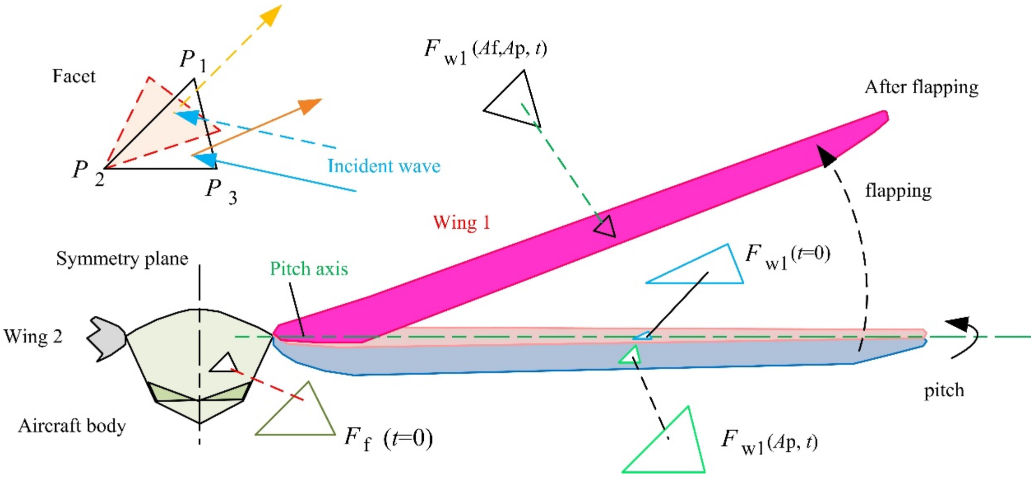

Figure 4. Schematic diagram of facet scattering when wing flapping.

When the wing starts flapping:

$$\boldsymbol{M}(F_{w1}(A_\mathrm{f}, A_\mathrm{p}, t)) = \begin{bmatrix} 1 & 0 & 0 \\ 0 & \cos A_{\mathrm{f1}}(t) & -\sin A_{\mathrm{f1}}(t) \\ 0 & \sin A_{\mathrm{f1}}(t) & \cos A_{\mathrm{f1}}(t) \end{bmatrix} \cdot \boldsymbol{M}^y(F_{w1}(A_\mathrm{p}, t)) \tag{28}$$

Noting the following relationship:

$$\boldsymbol{M}^y(F_{w1}(A_\mathrm{p}, t)) = \boldsymbol{M}(y(F_{w1}(A_\mathrm{p}, t)) - Y_{w1}) \tag{29}$$

where Y_{w1} denotes the distance from the flapping axis of wing 1 to the *xz* plane. The flapping axis of wing 1 is parallel to the *x*-axis and in the *xy* plane. According to the above steps, the pitching and flapping actions of wing 2 can also be transformed. Therefore, the dynamic matrix of the ornithopter can be updated as:

$$\boldsymbol{M}_{\mathrm{flap}}(t) = [\boldsymbol{M}_{\mathrm{w1}}(t), \boldsymbol{M}_{\mathrm{w2}}(t), \boldsymbol{M}_{\mathrm{f}}(t)] \tag{30}$$

Under the illumination of incident waves, the object surface is divided into a lighting area and a dark area:

$$\boldsymbol{M}(m_{\mathrm{flap}}(t)) = [\boldsymbol{M}(S_\mathrm{I}(t)), \boldsymbol{M}(S_D(t))] \tag{31}$$

where m_{flap} is the model of the flapping machine. $S_\mathrm{D}(t)$ denotes the dark area. $S_\mathrm{I}(t)$ refers to the illumination area, where more information is shown in papers [18,20]. For more details on the calculation framework, please refer to the reference [27], where the validation of the method can be found in the method section, and the comparison of different shapes of wings can be found in **Appendix A**.

The dimensions of this ornithopter are shown in **Table 1**, where the wing 1 and 2 adopt the same shape design and are symmetrical about the *xz* plane. L_f denotes fuselage length. W_f and H_f are the width and height of the fuselage, respectively. L_{ff} refers to the length of the front fuselage. L_{rf} means the length of the rear fuselage. W_{w1} is the distance from the apex of wing 1 outer end to the fuselage symmetrical plane. W_{rf} is the width of the fuselage tail, and W_{ff1} refers to a width parameter of the fuselage head.

Table 1. The size of the flapping machine.

Parameter	**L_f (m)**	**L_{ff} (m)**	**L_{rf} (m)**	**W_f (m)**
Value	1.6	0.35	0.95	0.2
Parameter	H_f (m)	W_{ff1} (m)	W_{w1} (m)	W_{rf} (m)
Value	0.1557	0.147	0.99	0.1

The validation of the RCS assessment method is shown in **Figure 5**, where the reference results are obtained from the output of PO + MOM/MLFMM (multilayer fast multipole method); at the same time, QSP is employed to handle the discrete state of wing flapping. It can be noticed that these two RCS curves are generally similar, while there are discrepancies in local fluctuations. The RCS mean indicator of the presented approach is −34.4751 dBm^2, which is 0.532 dBm^2 less than that of the comparison results. The error in this data comparison is mainly due to the difference in the calculation methods used for the two curves. At t = 1.01 s, the RCS value of the presented result is −33.18 dBm^2, while that of the reference data is equal to −30.69 dBm^2. For more detailed comparisons, please refer to **Table A1** in **Appendix A**. In addition, the performance of the two RCS curves is similar in terms of peak indicator and curve shape. These consequences show that the presented approach is feasible to compute the dynamic RCS of the flapping-wing.

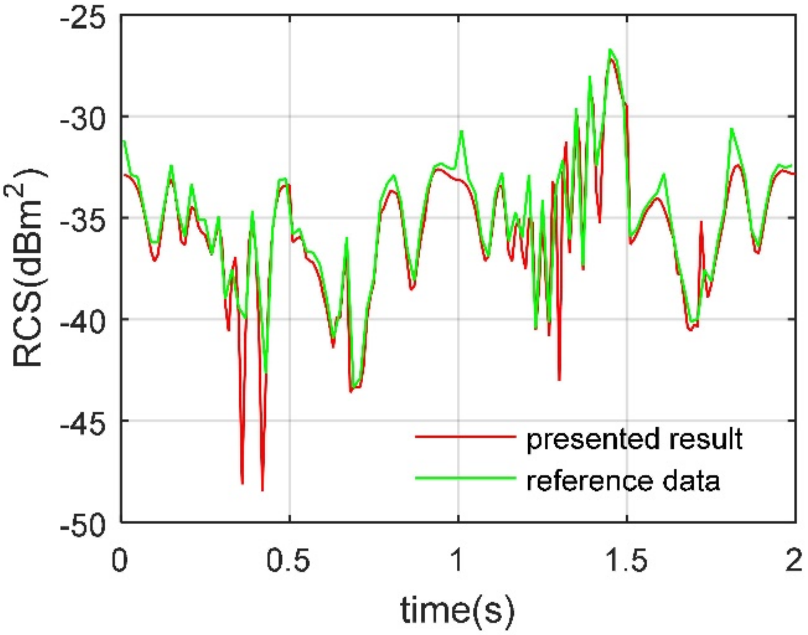

Figure 5. Verification of dynamic RCS calculation method for wing 1, f_{rh} = 7 GHz, α = 25°, β = 0°, flapping mode, A_{k1} = C_{k1} = 2π/45, ω_{k1} = ω_{k2} = 3.1416 rad/s, A_{k2} = C_{k2} = π/18, B_{k1} = B_{k2} = −π/2, θ_{up} = $-\theta_{\mathrm{down}}$ = 12°.

The RCS verification of the fuselage is presented in **Figure 6**, where this fuselage has a low level of electromagnetic scattering in the forward direction. The mean RCS indicator of the red curve based on the presented approach is −19.2137 dBm^2, where the RCS curve of the fuselage exhibits two large peaks in the lateral direction, reaching −0.3036 dBm^2. The mean RCS of the reference results based on PO+MOM is −18.557 dBm^2. Due to its slender and pointed design, the tail of the fuselage exhibits extremely low levels of electromagnetic scattering. These outcomes indicate that the presented approach is feasible and accurate for computing the RCS of the flapping machine.

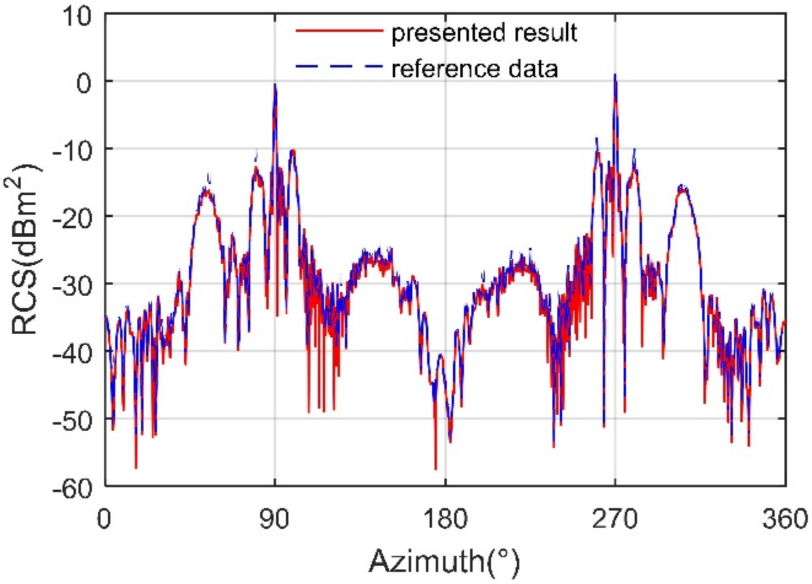

Figure 6. Verification of RCS calculation method for the fuselage, f_{rh} = 7 GHz, β = 10°.

3. Model Building

The ornithopter model is established as presented in **Figure 7**, where the whole aircraft presents a narrow and angular shape, with a slender tail, a sharp nose, and flat wings. In the initial state, both wings remain horizontal; that is, there are no pitching and flapping actions.

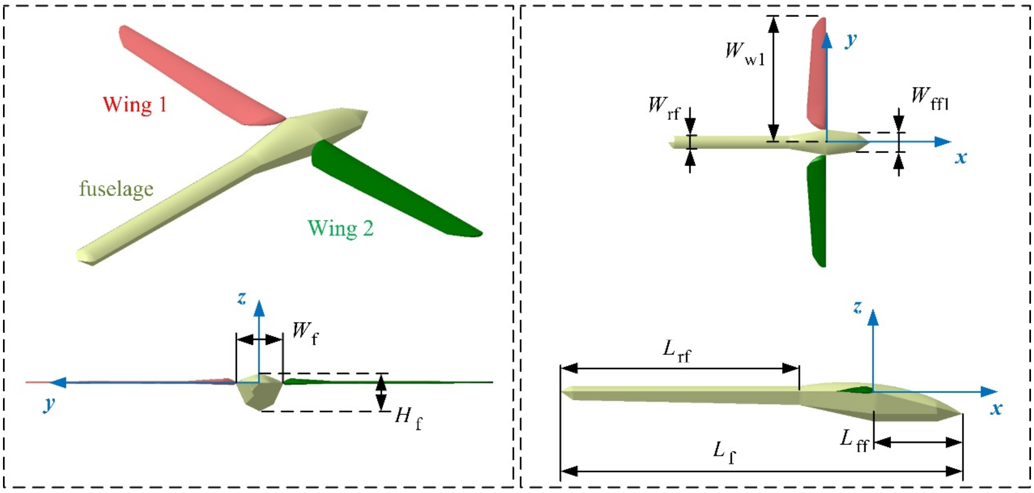

Figure 7. Model establishment of the biorobotics ornithopter.

The model details of wing 1 are presented in **Figure 8**, where H_{w1} denotes the maximum thickness of the wing, and C_{w11} stands for the maximum chord length of the wing. L_{w1} is the length of wing 1, and H_{w1t} denotes the thickness of the wing outer end. C_{w12} is a chord parameter of the wing near the tip. Y_{tv1} and Y_{tv2} are the distances from the two characteristic vertices of the trailing edge to the symmetry plane of the fuselage, respectively.

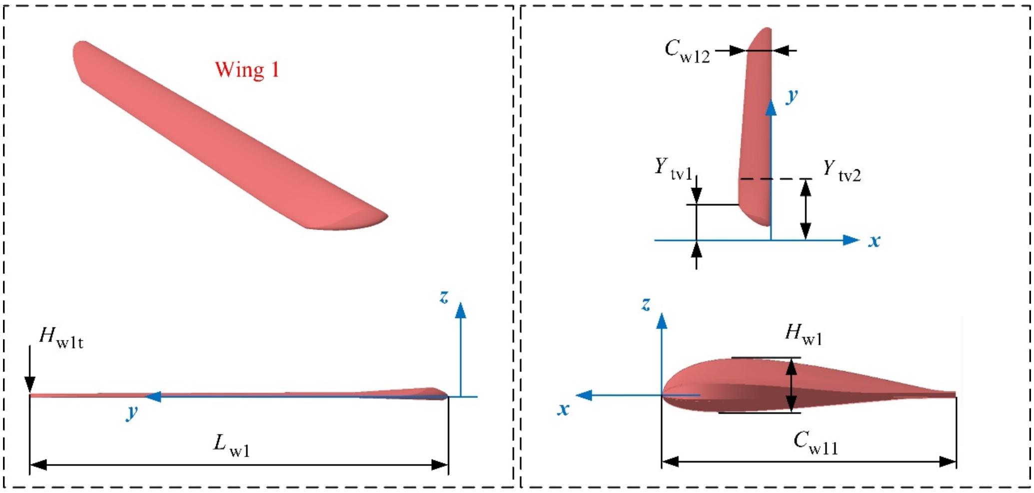

Figure 8. Model details of the wing 1.

The geometric dimensions of wing 1 are presented in **Table 2**, where Airfoil 1 stands for the airfoil applied in the cross-section of the wing. The wing is set as a rigid body model, which serves as the basis for subsequent research on two-stage, multi-stage, and flexible flapping wings. The entire wing is thin and streamlined, transitioning from a thick wing root to a flat wing tip.

Table 2. Wing 1 parameters.

Parameter	**L_{w1} (m)**	**C_{w11} (m)**	**Y_{tv1} (m)**	**C_{w12} (m)**
Value	0.86	0.15	0.195	0.108
Parameter	H_{w1t} (mm)	H_{w1} (mm)	Y_{tv2} (m)	Airfoil 1
Value	8.305	27.546	0.3	SM8016m

The surface of the ornithopter model is discretized into a large number of triangular meshes using high-accuracy unstructured mesh technology, as displayed in **Figure 9**, where small-sized edges and regions with large curvature changes are processed through mesh density increasing techniques. Rough grid division will affect the accuracy of **Figure 5** and related data calculations, where more verification and comparison can be found in reference [27]. Especially at the wing trailing edge, wingtip, and fuselage edge, the grid size is set at a low level as declared in **Table 3**, where the general minimum mesh size is set to 1 mm to reform grid quality near some edges.

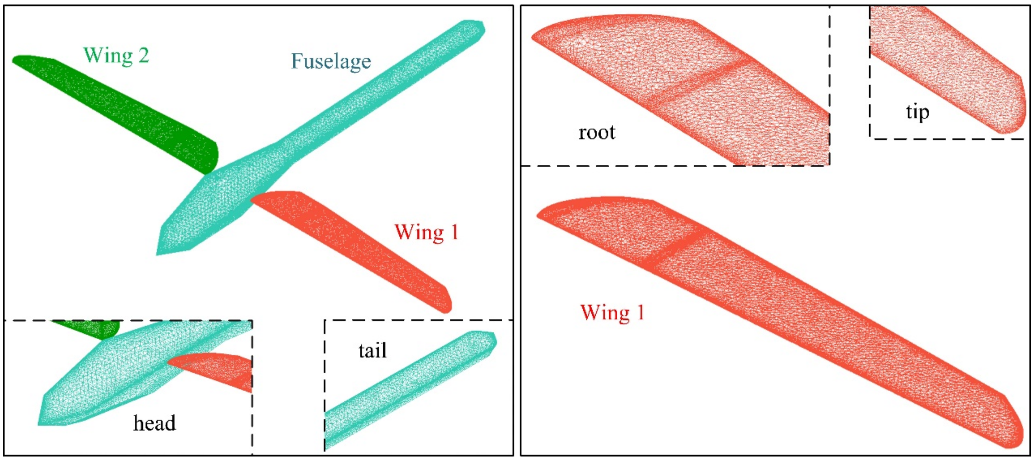

Figure 9. The mesh on the surface of the biorobotics ornithopter.

Table 3. Grid size of each part of the flapping machine.

Region	**Max Size (mm)**	**Region**	**Max Size (mm)**
wing trailing edge	1	wing leading edge	1
wing tip	2	wing root edge	2
fuselage side edge	2	bottom edge of fuselage	10
wing surface	8	fuselage surface	18

4. Results and Discussion

These research results mainly include three parts: remote sensing imaging analysis of ground and flapping wing aircraft, dynamic RCS and surface electromagnetic scattering features of ornithopter, and mixed analysis of remote sensing and RCS of low-altitude flapping-wing machine.

4.1. Remote Sensing Analysis

The remote sensing grayscale of the ground is presented in **Figure 10**, where the aircraft has not yet entered the observation zone. The grayscale distribution in the upper part of the picture is significantly lower than that in the lower part, where the grayscale around $x = 38.25$ m and $y = 19.832$ m appears black (grayscale less than -260). At $x = -26.36$ m and $y = -21.125$ m, there is a narrow raised slope with a grayscale of -122 located at the top of this mountain. Due to the setting of the elevation angle, the gray and black areas of reference objects such as mountains, circles, and trapezoids on the ground can be observed, and the relevant lengths and angles can be measured. These results indicate that this remote sensing approach is feasible for investigating the grayscale features of the observation area.

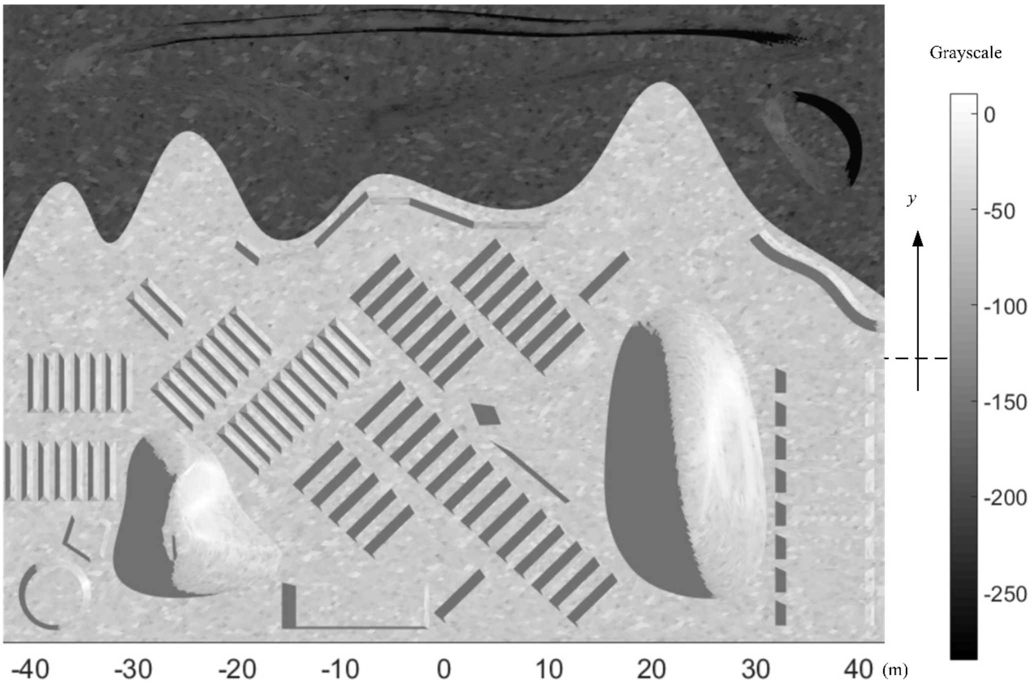

Figure 10. Grayscale image of remote sensing when this biorobotics ornithopter has not yet entered the observation area, f_{rh} = 5 GHz, α = 18°, β = 29°.

The grayscale features when the ornithopter flies into the designated region are presented in **Figure 11**, where a gray wing (grayscale from −28 to −52) is located above a dark gray ground trapezoid reference (grayscale of −135). The coordinate center of the picture has been transformed to the center of this target aircraft, where there are a total of 11 trapezoidal reference objects arranged diagonally near the projection of this aircraft (length 1.6 m). Due to the increase in elevation and azimuth angles observed by remote sensing, there has been a significant change in the grayscale distribution of the two mountain reference objects, where near x = 36.642 m and y = −3.425 m, there has been a significant reduction in the area of the dark gray region in the mountain. At x = −8.248 m and y = −8.119 m, the original dark gray narrow slope has transformed into light gray (grayscale −38) because of the increase in elevation angle of remote sensing. Due to the close grayscale between the projection of the fuselage (grayscale from −19 to −38) and the ground reference object (grayscale from −12 to −30) below it, the ornithopter in the figure can be fully observed after multiple local magnifications. Considering the contrast between the wing pointing outward towards the positive y-axis direction and the surrounding background, this contrast index can reach 76.

As presented in **Figure 12**, the flapping-wing machine is easily recognizable in contrast to low grayscale backgrounds. At x = −16.736 m and y = −40.89 m, a dark gray area remains near the bottom of the mountain reference object. Because water has a good absorption effect on microwaves, the gray level of water is much lower than that of wings and other reference objects on the ground. Around x = 26.335 m and y = 12.856 m, the gray level representation of the water here is obvious, ranging from gray (grayscale about −95) to dark gray (grayscale about −132) or even black (grayscale about −235). Although the width of the front fuselage is 0.2 m, the 0.95 m long tail beam and 0.86 m long wing (along with W_{w1} = 0.99 m) can still be observed. These results indicate that low grayscale water areas are advantageous for identifying this flapping wing.

As the azimuth of the remote sensing airship increases further, the gray and dark gray outlines of the reference objects arranged diagonally on the ground become more prominent, as shown in **Figure 13**. The coordinate center of the picture has been transformed to the center of this ornithopter, where the grayscale of the rear part of the fuselage is close to that of the long strip reference object below it. At y = −0.9609 m and x = 0.6318 m, the local grayscale of the long strip reference object is as low as −98, while the grayscale of a nearby wing surface is −72.

In the bottom left corner of the image, the top of the circular reference object is light gray (grayscale about −38) because of the increase in the elevation angle, and the edge slope is gray.

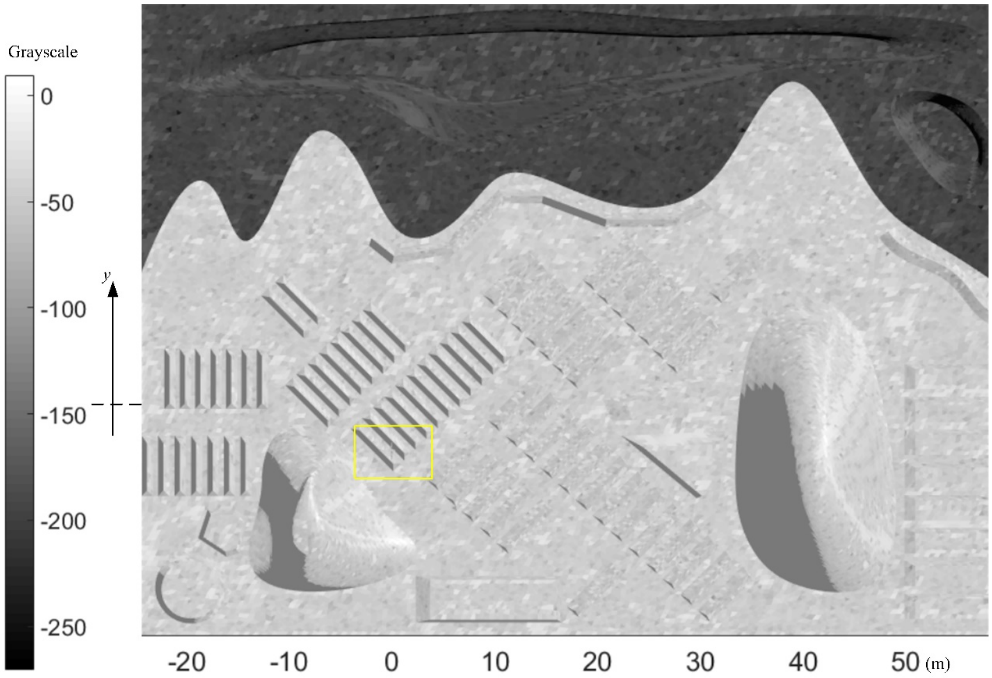

Figure 11. Grayscale image of the observation zone with the entry of the flapping machine, f_{rh} = 6 GHz, α = 30°, β = 50°.

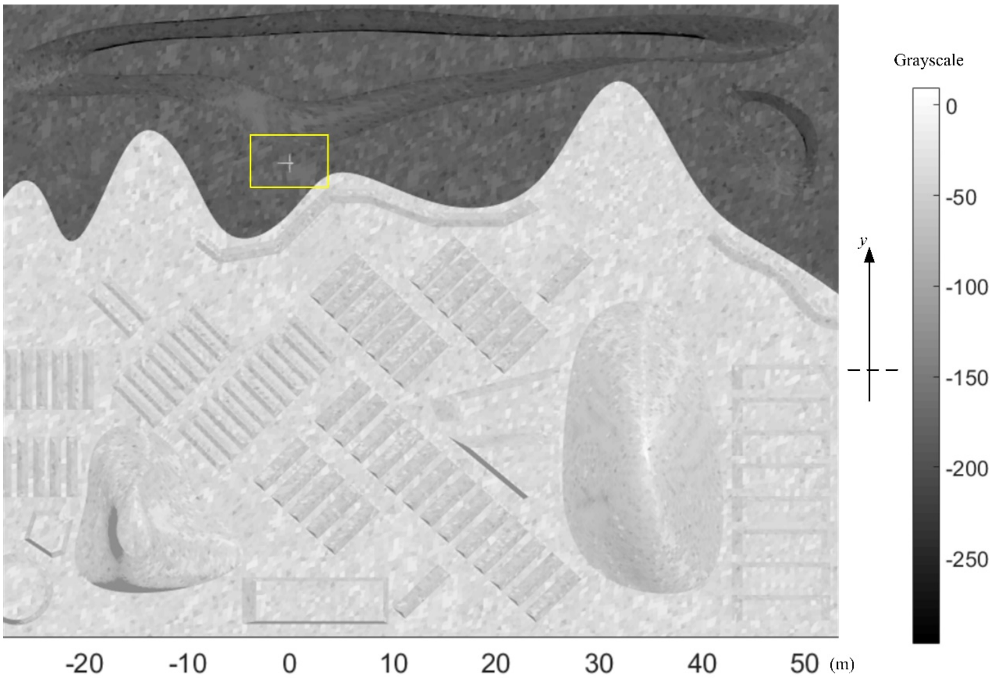

Figure 12. Grayscale image of remote sensing when the biorobotics ornithopter has entered the observation region, f_{rh} = 7 GHz, α = 52°, β = 66°.

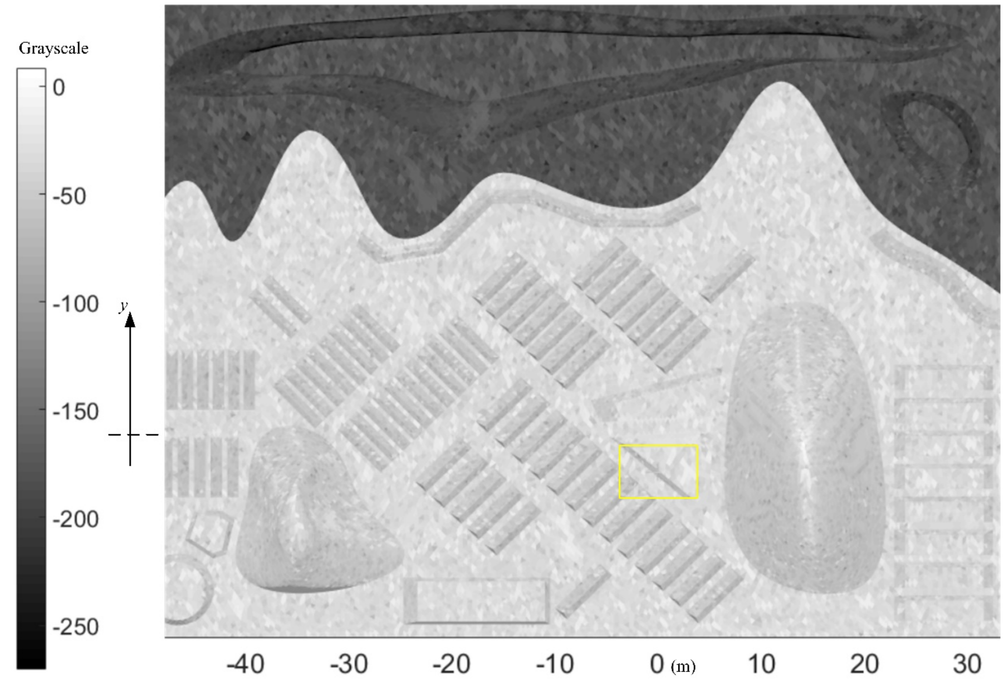

Figure 13. Grayscale image when the target aircraft has entered the observation area, f_{rh} = 8 GHz, α = 98°, β = 72°.

4.2. Dynamic RCS Analysis

Figure 14 presents that under the current circumstances, the average RCS result of this machine in the gliding mode generally decreases with the growth of the radar wave frequency. For the RCS at 2 GHz, the peak indicator of the curve is 2.366 dBm^2 occurring at 268.3° azimuth, and the mean is −11 dBm^2. As the radar frequency gradually extends from 4 GHz to 8 GHz, the mean RCS index declines from −14.0862 dBm^2 to −17.5284 dBm^2, because the specific shape of the aircraft is designed so that the high frequency characteristics of specular scattering do not dominate. While f_{rh} = 10 GHz, the average RCS gains to −17.2126 dBm^2, where that of the 12 GHz curve is −18.6536 dBm^2. The peak levels of these 6 RCS data lines are similar and appear in the lateral direction, because the slender side panels and edges of the ornithopter body provide many contributions. Based on the variation in the mean value of RCS, the edge diffraction contribution of this flapping machine is clearly evident. Due to the stealthy layout of the ornithopter body, the specular scattering of the fuselage is at a low level.

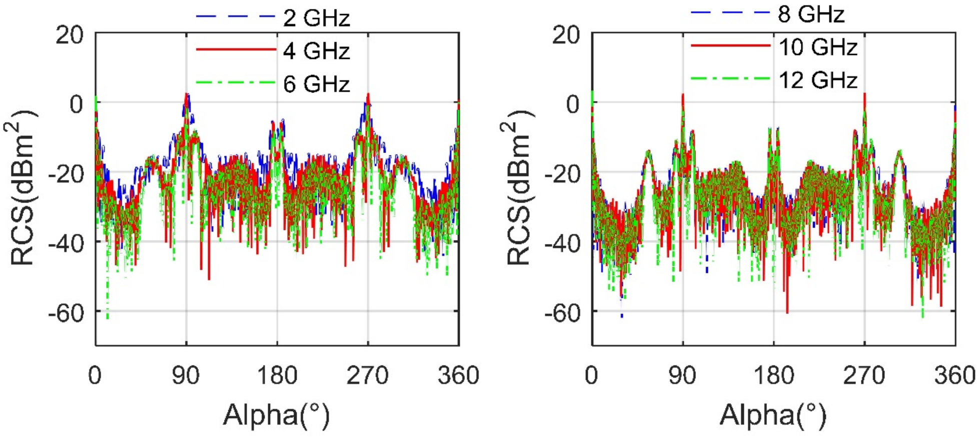

(**a**) (**b**)

Figure 14. RCS of the flapping wing aircraft, gliding mode, θ_0 = 3°, φ_0 = 8°, β = 0°. (**a**) RCS at 2, 4, 6 GHz; and (**b**) RCS at 8, 10, 12 GHz.

Figure 15 indicates that under the given observation angle, the mean RCS index of this ornithopter in flapping mode generally shows a downward trend. As the incident wave frequency gradually increases from 3 GHz to 7 GHz, the mean indicator of the RCS curve decreases from −23.6996 dBm^2 to −33.6183 dBm^2. At the same time, the peak reduces from −19.0349 dBm^2 to −25.9887 dBm^2, because the electromagnetism wave is incident from the front, the fuselage head and wing leading edge provide the main scattering contribution. In contrast, the fuselage head adopts a stealth design, and the scattering contribution of the leading edge of the wing changes continuously with the flap. When f_{rh} = 8 GHz, the RCS average grows to −33.1036 dBm^2, while the peak continues to decrease to −26.8704 dBm^2. It can be seen that the high-frequency features of specular scattering briefly dominate at this time. As the frequency continues to increase to 12 GHz, the RCS mean keeps decreasing until it reaches −37.1238 dBm^2, and the peak keeps decreasing until −31.9545 dBm^2. The results show that in the flapping mode, the impact of radar frequency on ornithopter RCS is also obvious, including curve shape, peak, and mean.

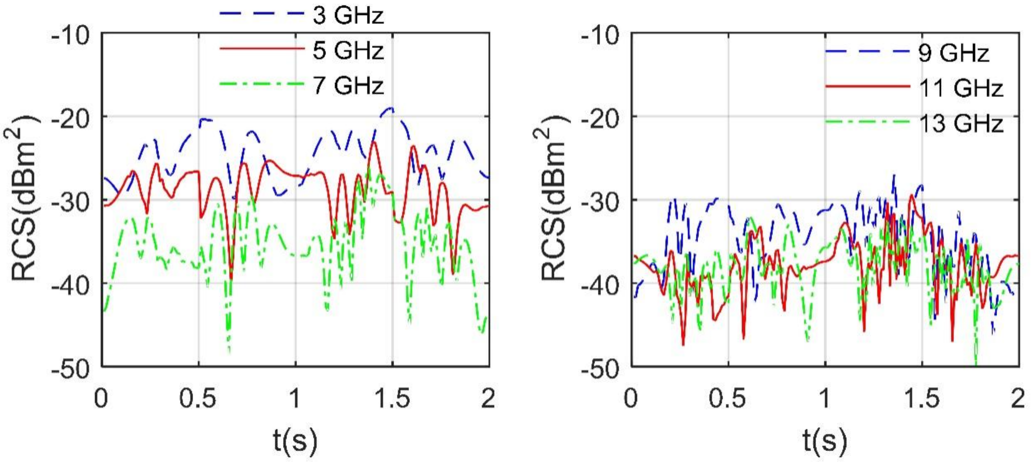

(**a**) (**b**)

Figure 15. Dynamic RCS of the flapping machine, flapping mode, $\theta_{\mathrm{up}} = -\theta_{\mathrm{down}} = 12°$, $A_{\mathrm{k2}} = C_{\mathrm{k2}} = \pi/18$, $A_{\mathrm{k1}} = C_{\mathrm{k1}} = 2\pi/45$, $\omega_{\mathrm{k1}} = \omega_{\mathrm{k2}} = 3.1416$ rad/s, $B_{\mathrm{k1}} = B_{\mathrm{k2}} = -\pi/2$, $\alpha = 20°$, $\beta = 5°$. (**a**) Results at 3, 5, 7 GHz; and (**b**) Results at 9, 11, 13 GHz.

Figure 16 shows that, at a fixed observation angle, the scattering characteristics of the aircraft surface change constantly with the flapping of the wings. The color bar on the right side of the image has a 1:1 mapping ratio to the facet RCS value. For the case of t = 0.1667 s, the nose exhibits more red areas, the rear fuselage displays a small amount of yellow-green distribution, and there are more orange-yellow areas around the edge of the tail. Because the radar wave is incident from the bottom and front, the wing upper surface is not in the direct irradiation area and appears blue. As time continues to increase to 0.5 s, both the pitch and flap angles of the wing increase, causing a small amount of orange and green to appear on the wing leading edge. When t = 0.8333 s, there are many orange and yellow areas on the wing upper surface, thanks to the downward flap of the wing and the change in pitch angle. Considering t = 1 s, although the wing remains horizontal, the presence of the pitching angle causes the front edge to point downward, causing the orange and yellow areas on the wing's upper surface to continue extending. As the time continued to increase to 1.4444 s, the wings kept flapping downward, making the wing 1 surface almost fully lit. When t = 1.6111 s, the wing is in the upward flapping stage, and the adjustment of the pitching angle makes the wing upper surface appear a large area of blue. The influence of wing elastic deformation on its electromagnetic scattering characteristics can be viewed in the attachment of reference [35]. These outcomes indicate that the changes in the scattering features of the ornithopter are obvious and non-negligible.

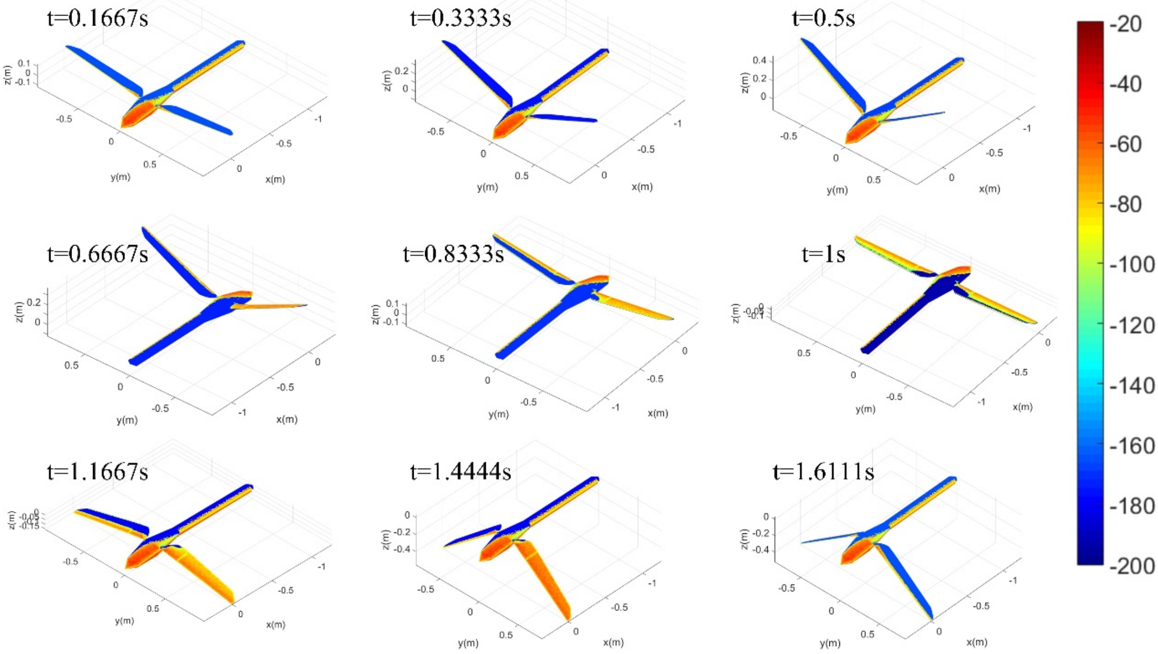

Figure 16. Surface scattering characteristics of the aircraft, f_{rh} = 8 GHz, flapping mode, $A_{\mathrm{k1}} = C_{\mathrm{k1}} = 2\pi/45$, $\omega_{\mathrm{k1}} = \omega_{\mathrm{k2}}$ = 3.1416 rad/s, $B_{\mathrm{k1}} = B_{\mathrm{k2}} = -\pi/2$, $\theta_{\mathrm{up}} = -\theta_{\mathrm{down}} = 12°$, $A_{\mathrm{k2}} = C_{\mathrm{k2}} = \pi/18$, $\alpha = 18°$, $\beta = -6°$, RCS unit; dBm^2.

Figure 17 shows that, under different forward incident waves, the dynamic RCS of this flapping machine exhibits significant differences, including curve shape, peak levels, and mean levels. Considering the curve at $\alpha = 5°$, the RCS mean index is −17.6881 dBm^2, and the peak index is −7.9833 dBm^2. As the azimuth gradually increases to 20°, the mean RCS keeps decreasing until it drops to −32.903 dBm^2, while the peak RCS is generally decreasing, recognizing that the peak of $\alpha = 20°$ curve is −27.6187 dBm^2. As the azimuth angle continues to grow to 30°, the mean RCS gradually extends to −27.5788 dBm^2, while the peak increases to −23.8292 dBm^2, because the scattering contribution from the machine body side increases. These results show that at a forward azimuth of 20°, the average and peak RCS of this ornithopter are lower compared to other example forward azimuths.

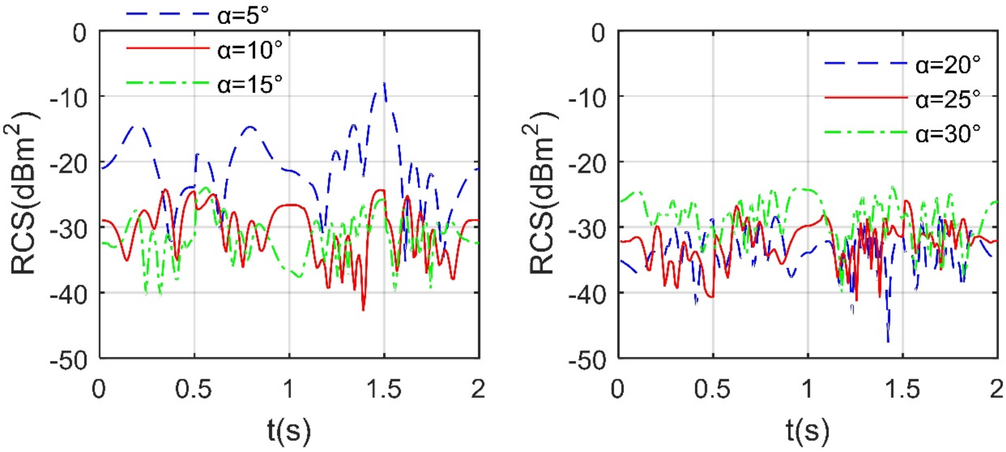

(**a**) (**b**)

Figure 17. Forward RCS of the ornithopter, f_{rh} = 8 GHz, flapping mode, $A_{\mathrm{k1}} = C_{\mathrm{k1}} = 2\pi/45$, $\omega_{\mathrm{k1}} = \omega_{\mathrm{k2}}$ = 3.1416 rad/s, $B_{\mathrm{k1}} = B_{\mathrm{k2}} = -\pi/2$, $A_{\mathrm{k2}} = C_{\mathrm{k2}} = \pi/18$, $\theta_{\mathrm{up}} = -\theta_{\mathrm{down}} = 12°$, $\beta = 0°$. (**a**) Case at α = 5°, 10°, 15°; and (**b**) Case at α=20°, 25°, 30°.

Figure 18 presents that the difference in the mean level of the ornithopter RCS for these given lateral azimuths is significant. As azimuth grows from 60° to 75°, the mean RCS index of the curve continuously declines from −19.4431 dBm^2 to −25.6098 dBm^2. The peak of the RCS curve at α = 70° is −22.1846 dBm^2, and that of the RCS curve at α = 75° is −21.9325 dBm^2. As the azimuth continues to increase to 85°, the RCS mean shows an increasing trend until it reaches −15.6082 dBm^2, while the peak continues to increase to −14.3575 dBm^2. It can be observed that within the range of 0.8667~1.122s, the six RCS curves exhibit similar shape characteristics, namely, they are generally flat. This is because the flap angle of the two wings is very small at this time, causing the wings to be in a nearly horizontal state. These consequences demonstrate that both the peak and mean indicators of the dynamic RCS curve for the ornithopter exhibit low levels at azimuths of 70° and 75° in these examples.

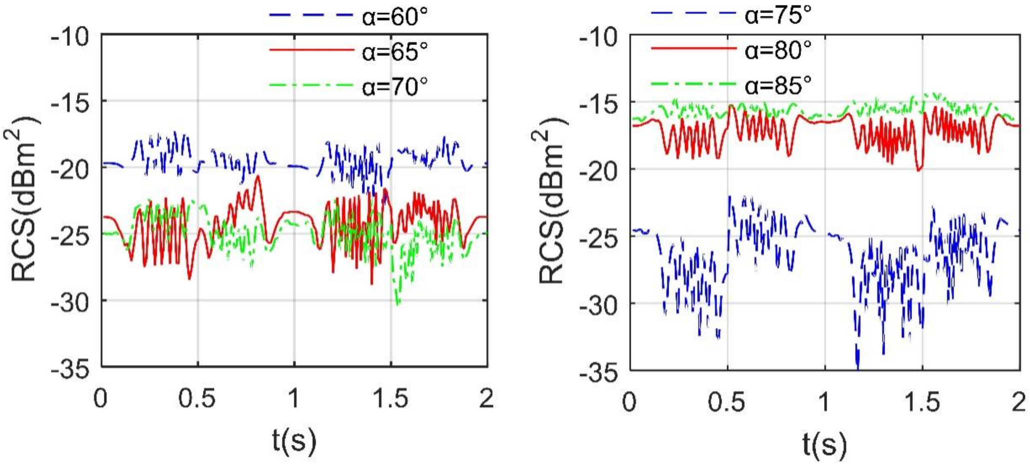

(**a**) (**b**)

Figure 18. Ornithopter dynamic RCS, flapping mode, $A_{\mathrm{k1}} = C_{\mathrm{k1}} = 2\pi/45$, $\theta_{\mathrm{up}} = -\theta_{\mathrm{down}} = 12°$, $\omega_{\mathrm{k1}} = \omega_{\mathrm{k2}} = 3.1416$ rad/s, $B_{\mathrm{k1}} = B_{\mathrm{k2}} = -\pi/2$, $A_{\mathrm{k2}} = C_{\mathrm{k2}} = \pi/18$, f_{rh} = 8 GHz, β = 0°. (**a**) RCS at α = 60°, 65°, 70°; and (**b**) RCS at α = 75°, 80°, 85°.

Figure 19 presents that under the current circumstances, when the azimuth exceeds 100°, the average RCS index of this flapping machine is greatly reduced. Considering the curve at α = 100°, the mean RCS is equal to −9.4736 dBm^2 as shown in **Table 4**, where the peak is −8.0433 dBm^2. For the other 5 RCS curves, the mean level is below −21.417 dBm^2, and the peak value is also less than −16.968 dBm^2. The reason for the large drop in RCS here is mainly due to the reduced contribution provided by the ornithopter body sides and wing outer ends. As the azimuth angle increases from 105° to 125°, there is a significant change in the shape of the RCS curve, while the RSC mean, fluctuation range, and peak level remain relatively unchanged. At these azimuths, although the contribution of specular reflections from the sides of the fuselage and the trailing edge of the wing is low, the dynamic changes due to wing flapping are noticeable. These results indicate that within the given range of lateral azimuths, maintaining a larger azimuth is beneficial to diminish the peak and mean RCS of this flapping machine.

Table 4. RCS record of the flapping-wing machine, flapping mode, $A_{\mathrm{k1}} = C_{\mathrm{k1}} = 2\pi/45$, $\omega_{\mathrm{k1}} = \omega_{\mathrm{k2}} = 3.1416$ rad/s, $\theta_{\mathrm{up}} = -\theta_{\mathrm{down}} = 12°$, $B_{\mathrm{k1}} = B_{\mathrm{k2}} = -\pi/2$, $A_{\mathrm{k2}} = C_{\mathrm{k2}} = \pi/18$, f_{rh} = 8 GHz, β = −10°, RCS unit: dBm^2.

	α = 100°	**α = 105°**	**α = 110°**	**α = 115°**	**α = 120°**	**α = 125°**
Mean	−9.4736	−21.9252	−24.7834	−21.4171	−22.3475	−22.3240
Peak	−8.0433	−18.3678	−20.6273	−16.9686	−17.4006	−18.2196

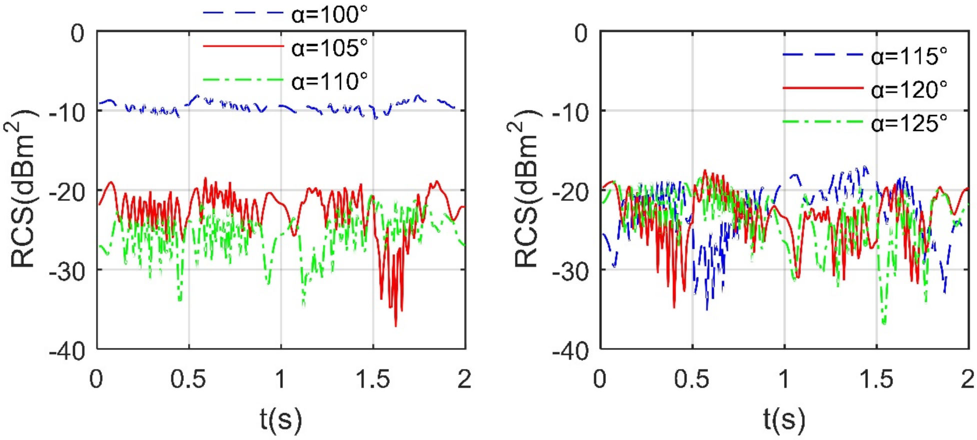

(**a**) (**b**)

Figure 19. Ornithopter side RCS, flapping mode, ω_{k1} = ω_{k2} = 3.1416 rad/s, B_{k1} = B_{k2} = −π/2, θ_{up} = $-\theta_{down}$ = 12°, A_{k1} = C_{k1} = 2π/45, A_{k2} = C_{k2} = π/18, β = −10°, f_{rh} = 8 GHz. (**a**) Example at α = 100°, 105°, 110°; and (**b**) Example at α = 115°, 120°, 125°.

4.3. Mixed Analysis

Figure 20 presents that under current conditions, the sides and bottom of the aircraft provide much scattering contributions to the trailing incident wave. Noticing the case of α = 160° and t = 0.3556 s, the flapping angle is 25.8506°, flapping upwards. Despite the pitching angle of the wing, the lower surface of wing 1 is still illuminated in yellow and orange. The lower skin of wing 2 is in the indirect irradiation area, and the upper skin is distributed with a large area of orange and yellow areas. The upper surface of wing 1 is mostly blue, with a small amount of yellow-green at the root of the wing. For the case of α = 190° and t = 1.3889 s, the wing is in the downward flapping period, and the flapping angle is 35.3209°. There is a small amount of green-yellow area on the back of the ornithopter's body, and the upper skin of the wing is almost all blue. Large areas of orange and red are distributed on the bottom of the fuselage, and the lower surfaces of the wings are depicted in varying shades of orange and yellow. As shown in reference [27], the dynamic scattering method based on PO+PTD can be used to study flapping wings of different shapes. These outcomes reveal that the flapping-wing can also exhibit strong scattering features under the illumination of the trailing incident wave.

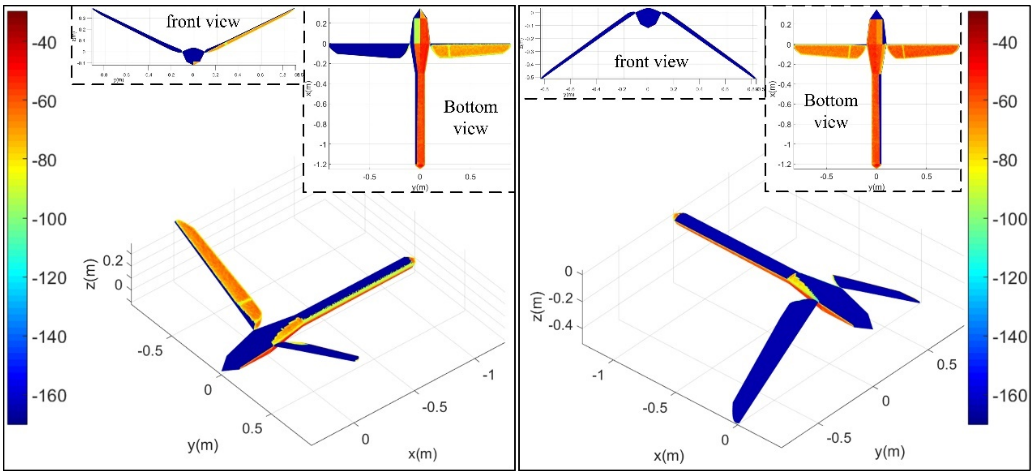

(**a**) (**b**)

Figure 20. Surface scattering characteristics of the ornithopter, flapping mode, ω_{k1} = ω_{k2} = 3.1416 rad/s, B_{k1} = B_{k2} = −π/2, A_{k1} = C_{k1} = 2π/45, θ_{up} = $-\theta_{down}$ = 12°, A_{k2} = C_{k2} = π/18, f_{rh} =8 GHz, β = −10°, RCS unit; dBm^2. (**a**) Sample at α = 160°, t = 0.3556 s; and (**b**) Sample at α = 190°, t = 1.3889 s.

Figure 21 shows that, within the given azimuth range, the peak RCS index of the ornithopter improves significantly as the azimuth increases. Considering the cases at α = 150°, 155°, and 160°, the shapes of the data curves are quite different, while the fluctuation range is analogous. The mean RCS decreases slowly from −26.6065 dBm^2 to −31.2860 dBm^2 as the azimuth grows from 150° to 160°, where the peak index declines from −21.2455 dBm^2 to −25.2322 dBm^2, as shown in **Table 5**. Compared to α = 100° in **Figure 19**, the mean RCS of α = 150° in **Figure 21** is 17.1329 dBm^2 lower. When the azimuth continues to increase to 175°, both the mean and peak value of the dynamic RCS curve maintain a continuous increasing trend, because the specular scattering of the convex surface of the fuselage tail and the contribution of the trailing edge of the wing are increasing. These results reveal that the peak and mean RCS performance of this ornithopter at 160° azimuth is favorable.

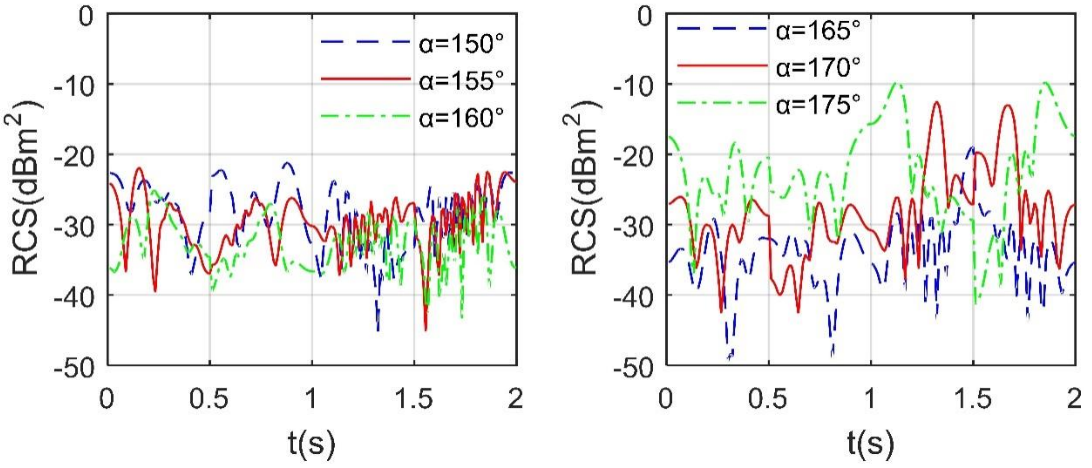

(**a**) (**b**)

Figure 21. Tail RCS of the flapping machine, flapping mode, $B_{\text{k1}} = B_{\text{k2}} = -\pi/2$, $A_{\text{k1}} = C_{\text{k1}} = 2\pi/45$, $\omega_{\text{k1}} = \omega_{\text{k2}} = 3.1416$ rad/s, $\theta_{\text{up}} = -\theta_{\text{down}} = 12°$, $A_{\text{k2}} = C_{\text{k2}} = \pi/18$, f_{rh} = 8 GHz, β = 10°. (**a**) Instance at α = 150°, 155°, 160°; and (**b**) Instance at α = 165°, 170°, 175°.

Table 5. RCS record of the ornithopter, f_{rh} = 8 GHz, flapping mode, $A_{\text{k1}} = C_{\text{k1}} = 2\pi/45$, $\omega_{\text{k1}} = \omega_{\text{k2}} = 3.1416$ rad/s, $\theta_{\text{up}} = -\theta_{\text{down}} = 12°$, $B_{\text{k1}} = B_{\text{k2}} = -\pi/2$, $A_{\text{k2}} = C_{\text{k2}} = \pi/18$, β = 10°, RCS unit: dBm^2.

	α = 150°	**α = 155°**	**α = 160°**	**α = 165°**	**α = 170°**	**α = 175°**
Mean	−26.6065	−28.0619	−31.2860	−30.8740	−23.1233	−18.1931
Peak	−21.2455	−21.8814	−25.2322	−19.0143	−12.5306	−9.6874

At y = 3.385 m and x = −65.592 m as shown in **Figure 22**, the water near this point appears as black gray (grayscale about −225) and black. Due to the increase in the emission frequency of remote sensing sensors, the grayscale of some ground reference objects tends to be light gray (grayscale from −18 to −25) overall. Around x = 0.3395 m and y = 1.956 m, the black gray, and black water background here allows the length of a wing to be measured. Because of the obvious grayscale layering of the water body, the length, width, and overall contour of the body can be observed through local magnification operations. At the current azimuth, the pitch motion of the wing cannot be directly captured in remote sensing images, while the RCS changes caused by flapping wings can exceed 26.8 dBm^2. In addition, the presence of rain or fog in actual situations causes scattering and absorption of light in the atmosphere, which affects the signal strength received by sensors. These outcomes demonstrate that the established approach is feasible for investigating the remote sensing and dynamic RCS of the ornithopter.

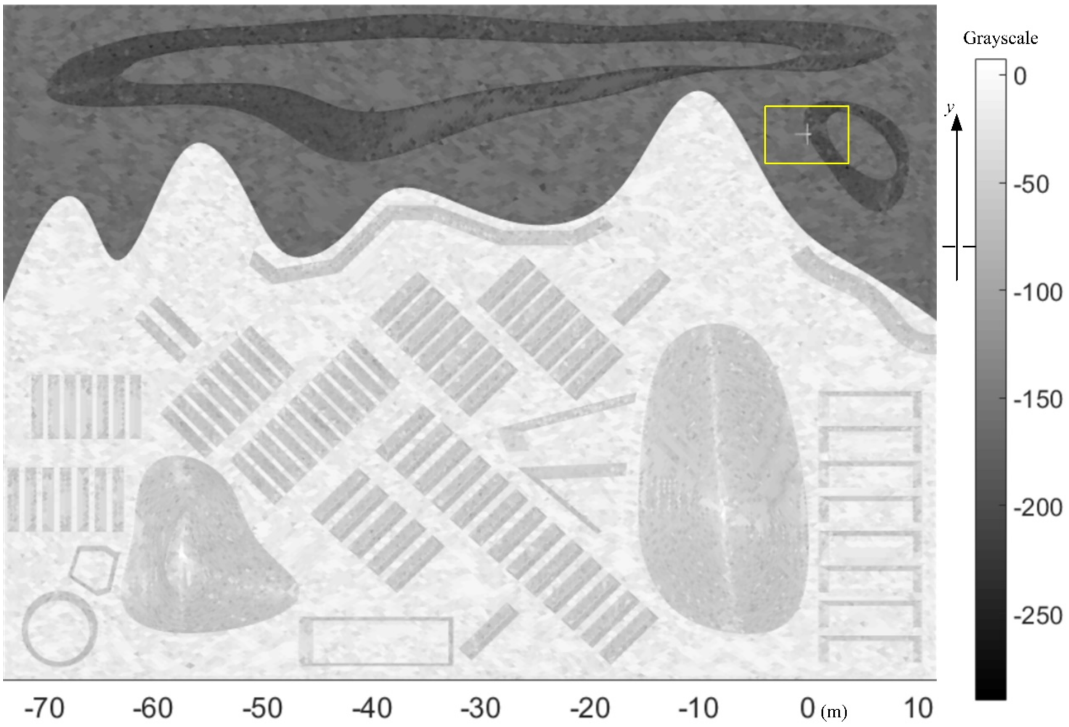

Figure 22. Grayscale image of remote sensing when the ornithopter has entered the sample region, f_{rh} = 9 GHz, α = 170°, β = 83°.

5. Conclusions

Based on the conjoint analysis method, the remote sensing grayscale pictures of the ground and the biorobotics ornithopter have been acquired, and the dynamic RCS of the ornithopter has been discussed. From these investigation analyses, the following key points can be summarized:

(1) This remote sensing approach can obtain the grayscale features of the ground, where the geometric dimensions of various-shaped reference objects can be measured. The grayscale of some complex ground reference objects is similar to that of the fuselage, making it difficult to quickly identify this flapping wing aircraft directly in remote sensing images.

(2) In a given radar wave frequency range, the mean and peak RCS indexes of the ornithopter generally show a downward trend with increasing frequency, while the high-frequency characteristics of the fuselage specular scattering do not dominate. For the forward incident waves in the given examples, there is an azimuth such that the mean and peak RCS indexes of this ornithopter are at low levels. While for the side cases, there are more examples of such favorable azimuths.

(3) The RCS mean of the tail direction case is overall lower than that of the side direction case, while the average and peak RCS of the former show a trend of first declining and then growing within the given range. Low gray water is advantageous for directly observing the flapping wing aircraft in remote sensing images, where the pitch motion of the wing cannot be reflected in the remote sensing image, while the RCS fluctuations caused by the wing motion are significant.

In future research, foldable wings and elastic structures will be an important direction for stealth analysis of flapping wing aircraft.

Author Contributions

Conceptualization, Z.Z. and J.H.; methodology, Z.Z. and J.H.; software, Z.Z.; validation, Z.Z.; formal analysis, Z.Z. and J.H.; investigation, Z.Z. and J.H.; writing—original draft preparation, Z.Z.; writing—review and editing, Z.Z. and

J.H.; visualization, Z.Z.; supervision, J.H.; funding acquisition, Z.Z. All authors have read and agreed to the published version of the manuscript.

Funding

The project was funded by China Postdoctoral Science Foundation (Grant Nos. BX20200035, 2020M680005).

Institutional Review Board Statement

Not applicable.

Informed Consent Statement

Not applicable.

Data Availability Statement

Some or all data, models, or code that support the findings of this study are available from the corresponding author upon reasonable request.

Conflicts of Interest

The authors declare that there is no conflict of interest.

Appendix A

The two methods are based on the same flapping wing model, and the initial grid generation time is the same, as shown in **Table A1**, where the biggest difference is the time consumed for grid updates when the number of data nodes for the dynamic RCS curve is 180.

Table A1. Comparison of time consumption between the presented method and traditional methods.

	Modeling	Grid Initialization	Grid Updating	Calculating
Presented method	1 h	30 min	2.16 min	4.1667 min
MOM+QSP	1 h	30 min	323 min	6.76 min

References

1. Bevidran, N. Swarm Robotics in Agriculture: Collective Behaviour for Precision Farming. *Bio-Robotics* **2025**, *1*, 55–69.
2. Xiao, S.; Hu, K.; Huang, B.; et al. A Review of Research on the Mechanical Design of Hoverable Flapping Wing Micro-Air Vehicles. *J. Bionic Eng.* **2021**, *18*, 1235–1254.
3. Bluman, J.E.; Pohly, J.A.; Sridhar, M.K.; et al. Achieving Bioinspired Flapping Wing Hovering Flight Solutions on Mars via Wing Scaling. *Bioinsp. Biomim.* **2018**, *13*, 046010.
4. Fu, Y.; Zhao, S. Design of the Aircraft Model for Bionic Dragonflies' Flapping Wings and Analysis on the Aerodynamic Characteristics. *J. Mach. Des.* **2021**, *38*, 79–87.
5. Shyy, W.; Aono, H.; Chimakurthi, S.K.; et al. Recent Progress in Flapping Wing Aerodynamics and Aeroelasticity. *Prog. Aerosp. Sci.* **2010**, *46*, 284–327.
6. Kumar, A.; Kumar, N.; Das, R.; et al. In Vivo Structural Dynamic Analysis of the Dragonfly Wing: The Effect of Stigma as Its Modulator. *Philos. Trans. R. Soc. A* **2019**, *377*, 20190132.
7. Jiao, Z.; Wang, L.; Zhao, L.; et al. Hover Flight Control of X-Shaped Flapping Wing Aircraft Considering Wing–Tail Interactions. *Aerosp. Sci. Technol.* **2021**, *116*, 106870.
8. Peng, C.; Sun, L.; Wang, Y.; et al. Control Oriented Longitudinal Modeling and Analysis of Pigeon-Like Flapping-Wing Aircraft. *J. Beijing Univ. Aeronaut. Astronaut.* **2021**, *48*, 2510–2519.

9. Bie, D.; Li, D.; Xiang, J.; et al. Design, Aerodynamic Analysis and Test Flight of a Bat-Inspired Tailless Flapping Wing Unmanned Aerial Vehicle. *Aerosp. Sci. Technol.* **2021**, *112*, 106557.
10. Zhong, Y.; Wu, J.; Lin, Z.; et al. Design of a Two-Stage Flapping Wing Bionic Aircraft. *Electromech. Eng. Technol.* **2021**, *50*, 9–12. (in Chinese)
11. Zhou, Z.; Huang, J. Numerical Investigations on Radar Cross-Section of Helicopter Rotor with Varying Blade Pitch. *Aerosp. Sci. Technol.* **2022**, *123*, 107452.
12. Shen, H.; Yu, Y. Development and Key Technologies of Morphological Bionic Aircraft. *Adv. Aeronaut. Sci. Eng.* **2021**, *12*, 9–19. (in Chinese)
13. Zhou, Z.; Huang, J. X-Band Radar Cross-Section of Tandem Helicopter Based on Dynamic Analysis Approach. *Sensors* **2021**, *21*, 271.
14. Knott, E. RCS Reduction of Dihedral Corners. *IEEE Trans. Antennas Propag.* **1977**, *25*, 406–409.
15. Jiang, Z.H. Research on Radar Target Characteristics of Unmanned Helicopter. *J. Astronaut. Metrol. Meas.* **2015**, *35*, 61–66.
16. Maffett, A.L. *Topics for a Statistical Description of Radar Cross Section*. Wiley-Interscience: New York, NY, USA, 1989.
17. Ye, S.B.; Xiong, J.J. Dynamic RCS Behavior of Helicopter Rotating Blades. *Acta Aeronaut. Astronaut. Sin.* **2006**, *27*, 816–822.
18. Zhou, Z.; Huang, J.; Wang, J. Compound Helicopter Multi-Rotor Dynamic Radar Cross Section Response Analysis. *Aerosp. Sci. Technol.* **2020**, *105*, 106047.
19. Nguyen, K.; Au, L.T.K.; Phan, H.V.; et al. Effects of Wing Kinematics, Corrugation, and Clap-and-Fling on Aerodynamic Efficiency of a Hovering Insect-Inspired Flapping-Wing Micro Air Vehicle. *Aerosp. Sci. Technol.* **2021**, *118*, 106990.
20. Zhou, Z.; Huang, J. Study of RCS Characteristics of Tilt-Rotor Aircraft Based on Dynamic Calculation Approach. *Chin. J. Aeronaut.* **2022**, *34*, 426–437.
21. Guo, J.; Yin, H.C.; Ye, S.J.; et al. Novel Technology for Electromagnetic Characteristic Simulation of Helicopter Blades. *Acta Aeronaut. Astronaut. Sin.* **2019**, *40*, 322732.
22. Zhou, Z.; Huang, J. An Optimization Model of Parameter Matching for Aircraft Catapult Launch. *Chin. J. Aeronaut.* **2020**, *33*, 191–204.
23. Ruiz, C.; Acosta, J.Á.; Ollero, A. Aerodynamic Reduced-Order Volterra Model of an Ornithopter under High-Amplitude Flapping. *Aerosp. Sci. Technol.* **2022**, *121*, 107331.
24. Takahashi, T. A Fast Time-Domain Boundary Element Method for Three-Dimensional Electromagnetic Scattering Problems. *J. Comput. Phys.* **2023**, *482*, 112053.
25. Abbasi, S.H.; Mahmood, A.; Khaliq, A. Bioinspired Feathered Flapping Wing UAV Design for Operation in Gusty Environment. *J. Robot.* **2021**, *2021*, 8923599.
26. Ma, Y.; Karpuk, S.; Elham, A. Conceptual Design and Comparative Study of Strut-Braced Wing and Twin-Fuselage Aircraft Configurations with Ultra-High Aspect Ratio Wings. *Aerosp. Sci. Technol.* **2022**, *121*, 107395.
27. Zhou, Z.; Huang, J. Utilizing Dynamic Scattering for Learning Radar Cross-Section of a Flapping-Wing Aircraft. *Photonics* **2022**, *9*, 877.
28. Quintana, A.; Graves, G.; Hassanalian, M.; et al. Aerodynamic Analysis and Structural Integrity for Optimal Performance of Sweeping and Spanning Morphing Unmanned Air Vehicles. *Aerosp. Sci. Technol.* **2021**, *110*, 106458.
29. Ammari, H.; Bao, G.; Wood, A. A Cavity Problem for Maxwell's Equations. *Methods Appl. Anal.* **2002**, *9*, 249–260.
30. Lee, J.; Yoon, S.H.; Kim, C. Experimental Surrogate-Based Design Optimization of Wing Geometry and Structure for Flapping Wing Micro Air Vehicles. *Aerosp. Sci. Technol.* **2022**, *123*, 107451.
31. Singh, S.; Zuber, M.; Hamidon, M.N.; et al. Classification of Actuation Mechanism Designs with Structural Block Diagrams for Flapping-Wing Drones: A Comprehensive Review. *Prog. Aerosp. Sci.* **2022**, *132*, 100833.
32. Zhou, Z.; Huang, J. Study of the Radar Cross-Section of Turbofan Engine with Biaxial Multirotor Based on Dynamic Scattering Method. *Energies* **2020**, *13*, 5802.
33. Zhou, Z.; Huang, J. Y-Type Quadrotor Radar Cross-Section Analysis. *Aircr. Eng. Aerosp. Technol.* **2023**, *95*, 535–545.
34. Silva, R.C.; Bueno, D.D. On the Dynamics of Flexible Wings for Designing a Flapping-Wing UAV. *Drones* **2024**, *8*, 56.

35. Zhou, Z.; Huang, J. Z-Folding Aircraft Electromagnetic Scattering Analysis Based on Hybrid Grid Matrix Transformation. *Sci. Rep.* **2022**, *12*, 4452.
36. Xue, Y.; Cai, X.; Liu, H. Aerodynamics and Stability of Hawkmoth Forward Flight with Flexible Wing Hinge. *Phys. Rev. Fluids* **2024**, *9*, 063101.